Temperature inversions, thermal tides, and water ice clouds in the Martian tropics

D. P. Hinson

Department of Electrical Engineering, Stanford University, Stanford, California, USA

R. J. Wilson

Geophysical Fluid Dynamics Laboratory/NOAA, Princeton University, Princeton, New Jersey, USA

[1] We report new results on the structure and dynamics of the tropical atmosphere of Mars derived from a combination of radio occultation measurements by Mars Global Surveyor and simulations by a Mars general circulation model (MGCM). Radio occultation experiments sounded the equatorial atmosphere at latitudes of 36°N to 30°S during midsummer of the Northern Hemisphere ($L_s = 134°-162°$), sampling the predawn thermal structure at a local time of ~0412. Elevated temperature inversions are a conspicuous feature of these observations. They appear at pressures between 30 and 200 Pa, well above the surface, and their magnitude exceeds 6 K in 34% of the temperature profiles in this latitude band. The properties and spatial distribution of these elevated inversions are organized across the tropics on planetary scales. Inversions are strongest and occur most frequently above elevated terrain, achieving a peak magnitude of ~30 K near Tharsis, and their altitude generally increases toward the south. According to MGCM simulations, which closely resemble the observations, these temperature inversions arise from zonally modulated thermal tides. The best simulation includes an interactive hydrologic cycle, which results in strong coupling between the thermal tides and radiatively active water ice clouds. Prominent clouds form in response to wave-induced adiabatic cooling and evolve in a pattern closely correlated with the thermal structure of the tides. The tides in turn are intensified by radiative forcing from the clouds. This tide-cloud coupling imposes strong diurnal modulation on the properties of clouds in the tropics. *INDEX TERMS:* 5409 Planetology: Solid Surface Planets: Atmospheres—structure and dynamics; 3346 Meteorology and Atmospheric Dynamics: Planetary meteorology (5445, 5739); 5445 Planetology: Solid Surface Planets: Meteorology (3346); 6225 Planetology: Solar System Objects: Mars; 3384 Meteorology and Atmospheric Dynamics: Waves and tides; *KEYWORDS:* Mars, Mars Global Surveyor, atmospheric dynamics, thermal tides, water ice clouds

1. Introduction

[2] This is the third in a series of papers concerning radio occultation experiments conducted in May–June 1999 as part of the Radio Science (RS) investigation of Mars Global Surveyor (MGS). Previous papers focused on extratropical dynamics during southern winter, including both transient eddies [*Hinson and Wilson*, 2002] and stationary planetary waves [*Hinson et al.*, 2003]. We now turn our attention to the thermal structure and dynamics of the equatorial atmosphere.

[3] These radio occultations systematically sounded the predawn thermal structure throughout the tropics, yielding 440 atmospheric profiles with exceptional accuracy and vertical resolution. The season was midsummer of the Northern Hemisphere ($L_s = 134°-162°$). A subset of these

RS profiles is distinguished by the presence of remarkably strong temperature inversions at pressures of about 50–100 Pa. The RS data provide an intriguing characterization of these inversions, as described in section 2, but their nature and origin are difficult to deduce from the RS observations alone.

[4] As in previous papers in this series, we supplement the RS measurements with simulations by the Mars general circulation model (MGCM) of the NOAA Geophysical Fluid Dynamics Laboratory (GFDL) [*Wilson and Hamilton*, 1996]. Comparisons of simulations with key features of the RS data, such as the strong tropical temperature inversions described here, offer guidance toward improving the accuracy and reliability of the MGCM. Once an accurate simulation has been achieved, the MGCM in turn offers deeper insight into the behavior of the atmosphere.

[5] In this paper we use the GFDL MGCM to explore the coupled behavior of thermal tides and water ice clouds, with
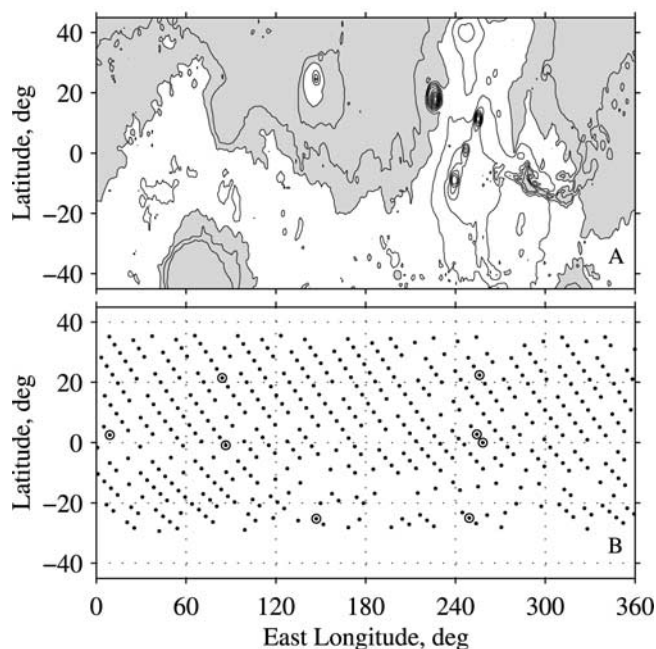
Figure 1. (a) Martian topography [*Smith et al.*, 2001]. Shading denotes negative elevation. The contour interval is 2.5 km. (b) Distribution of RS measurements. Circles mark the locations of the profiles shown in Figure 2.

emphasis on understanding the factors that lead to the formation of elevated temperature inversions. This is a logical extension of previous modeling studies, which have shown that tropical temperature inversions can arise either dynamically from zonally modulated thermal tides [e.g., *Hinson and Wilson*, 2000; *Wilson et al.*, 2003] or radiatively from a water ice cloud layer [e.g., *Haberle et al.*, 1999; *Colaprete and Toon*, 2000]. Our simulations provide the first self-consistent treatment of both phenomena, which proves to be a crucial step toward understanding not only the observed inversions but also the behavior of tropical water ice clouds. The importance of this approach is reflected in the strong radiative-dynamical coupling between tides and water ice clouds that characterizes our best simulation.

[6] Some interaction between tropical tides and clouds is likely to occur at this season. A prominent band of water ice clouds appears at latitudes of about 10°S–30°N during spring and summer of the Northern Hemisphere [e.g., *Clancy et al.*, 1996; *Smith et al.*, 2001b; *Wang and Ingersoll*, 2002; *Smith*, 2004]. Near $L_s = 150°$, the cloud base is ~15 km above the surface during daytime [*Smith*, 2002]. Within this context, thermal tides will modulate the height of the condensation level, which is extremely sensitive to temperature variations. Our MGCM simulations are designed to explore this interaction. We find that tidal temperature variations strongly influence the spatial structure and time evolution of tropical clouds.

2. Radio Occultation Measurements

2.1. Experiment Description

[7] Radio occultation experiments are conducted routinely with MGS to monitor the structure and dynamics of the

neutral atmosphere [*Tyler et al.*, 2001]. Each observation yields a profile of temperature and geopotential versus pressure that extends from the surface to ~10 Pa, an altitude interval of ~40 km. More than 8000 RS profiles have been retrieved since measurements began in January 1998, and these experiments are continuing as part of an ongoing extended mission.

[8] We consider a set of 440 RS profiles of the tropical atmosphere obtained in May–June 1999, which corresponds to northern summer of Mars year 24 (MY 24). (In this convention for counting Martian years, MY 1 begins at $L_s = 0°$ on 11 April 1955 [*Clancy et al.*, 2000]). These RS profiles are most accurate near the surface and least accurate at high altitudes. Typical values for the standard deviation in temperature are ~5 K at 25 Pa, ~2 K at 100 Pa, and ~1 K at 400 Pa. The vertical resolution of these profiles is ~500 m. Additional discussion of the method of data analysis and the characteristics of the resulting profiles is given by *Hinson et al.* [1999, 2001].

[9] Figure 1 shows the spatial distribution of the RS profiles, which forms a regular pattern across the tropics. Occultation experiments were generally performed in the northern tropics on every spacecraft orbit. The separation in longitude between consecutive profiles is 28.6°, providing daily sampling of zonal structure through wave number 6. Measurements at intervals of 25 orbits (~49 h) form diagonals sloping from upper left to lower right in Figure 1b. The measurements drifted steadily in latitude from 36°N at $L_s = 134°$ to 30°S at $L_s = 162°$. The local time remained within a narrow range (0407–0426), preceding sunrise by ~1 hour. Relatively few RS profiles are available in the southern tropics at 120°–330°E.

[10] Two types of ambiguity are inherent in these RS measurements. First, the local time of the measurements is essentially constant, causing aliasing in observations of thermal tides. Second, the measurements move slowly in latitude, requiring ~28° of L_s to progress from 36°N to 30°S, so that variations with latitude are difficult to separate from variations with L_s. We will rely on MGCM simulations for guidance in resolving these ambiguities.

2.2. RS Results

[11] Figure 2 shows pairs of profiles at four selected latitudes, which illustrate characteristics of the predawn thermal structure observed in the tropics. The base of each profile lies within a few hundred meters of the surface, and the variations in surface pressure are due primarily to topography. Each profile contains a temperature inversion in the lowest few kilometers above the ground that results from nighttime cooling of the surface [cf. *Hinson et al.*, 1999, Plate 2].

[12] A different type of inversion, highly variable in magnitude, appears well above the surface in all eight profiles of Figure 2. Consider the case at 3°N (Figure 2b). The profile at 254°E, above Tharsis, includes a remarkable inversion with temperature increasing from 161 K at 90 Pa to 192 K at 50 Pa. This contrasts sharply with the inversion at 9°E, which is comparatively weak. Profiles measured 2 days later at the equator exhibit similar features (Figure 2c).

[13] The dashed line in Figure 2c is the adiabatic temperature gradient. Both profiles contain a layer of neutral
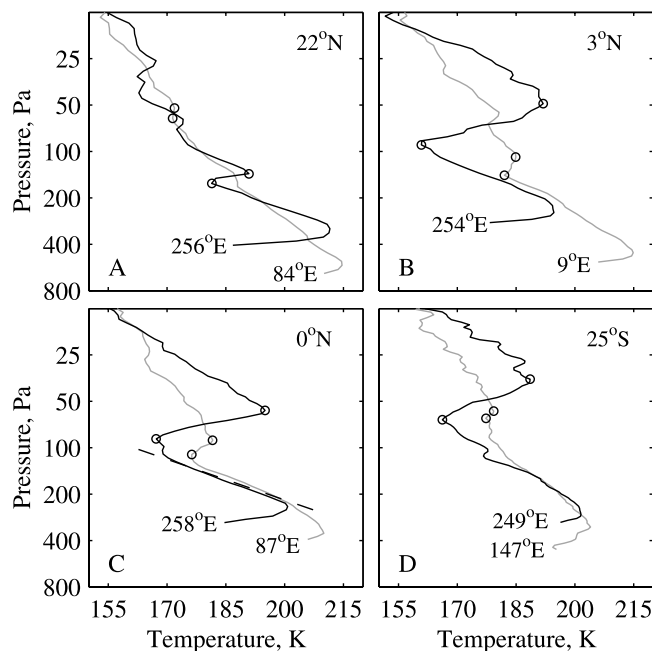
Figure 2. Selected RS profiles at (a) 22°N, $L_s = 140°$, (b) 3°N, $L_s = 147°$, (c) 0°N, $L_s = 148°$, and (d) 25°S, $L_s = 159°$. The interval between each pair of measurements is <18 h. These profiles are at locations (dark) above Tharsis and (light) at other longitudes, as indicated in Figure 1b. Circles denote the base and peak of the strongest elevated temperature inversion in each profile. The dashed line in (c) shows the adiabatic temperature gradient.

static stability at pressures near 150 Pa sandwiched between the near-surface and elevated temperature inversions, where the static stability is large.

[14] We developed automated software that scans all 440 RS profiles and identifies the strongest temperature inversion (if any) within each profile. This algorithm ignores the boundary-layer inversion adjacent to the surface as well as inversions at pressures less than 20 Pa, where the measurement uncertainties are relatively large. Tabulated results include the temperature and pressure at both the base and the peak of the inversion. These features are identified by circles for the eight profiles in Figure 2.

[15] Figure 3 maps the observed temperature inversions in latitude, longitude, and magnitude ΔT. There is a noticeable correlation between this distribution and the underlying surface topography (Figure 3a). Inversions are strongest and occur most frequently above elevated terrain, while few notable inversions appear over the low-lying planitia of the northern tropics (e.g., Isidis, Utopia, Amazonis, and Chryse). As a result of this correlation with topography, the distribution of inversions varies distinctively with both longitude and latitude.

[16] The strongest inversions ($\Delta T > 18$ K) are confined (with one exception) to longitudes of 220°–270°E, above Tharsis (Figure 3a). Moderate inversions ($\Delta T = 12$–18 K) are more widely distributed. They appear above Tharsis in the region surrounding the strongest inversions, in a

cluster at 300°–330°E, and sporadically at 0°–160°E. Inversions with $\Delta T > 6$ K occur most frequently above Tharsis and least frequently at 160°–200°E, as shown in Figure 3b.

[17] The distribution of these inversions is asymmetric about the equator. (According to the MGCM simulation discussed in section 4, this asymmetry reflects meridional structure rather than variation with L_s.) Inversions exceeding 6 K occur frequently in the southern tropics (Figure 3a) but are relatively scarce in the north except near Tharsis. Stronger inversions ($\Delta T > 12$ K) are absent at latitudes north of 11°N but appear as far south as 27°S.

[18] The structure of the inversions varies with latitude in another important respect. This point is illustrated in Figure 4, which shows the location in latitude and pressure of selected inversions. At longitudes of 210°–270°E (Figure 4a), the height of the inversions tends to increase from relatively low altitudes in the northern tropics to higher altitudes in the south. This effect is also apparent in Figure 2. In the profiles at 249°–258°E, above Tharsis, the pressure at the base of the inversion decreases from 160 Pa at 22°N to 65 Pa at 25°S, corresponding to an increase in geopotential height of ~9 km. The inversions on the
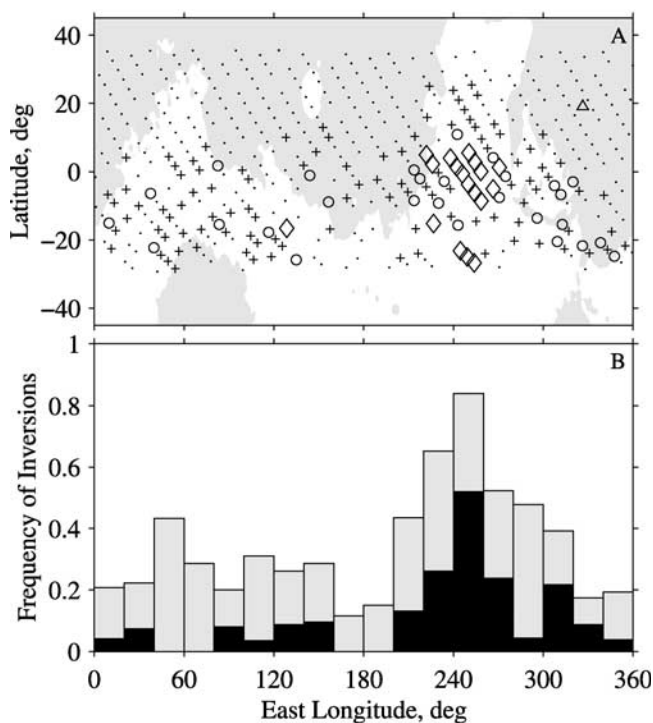
Figure 3. (a) Distribution of tropical temperature inversions. Symbols show locations where RS profiles contain elevated inversions of (plus) 6–12 K, (circle) 12–18 K, and (diamond) >18 K. Inversions are weaker or absent at locations shown by black dots. A triangle marks the Mars Pathfinder landing site. Gray shading denotes negative surface elevation, as in Figure 1. (b) A histogram showing the fraction of RS profiles that contains an inversion larger than (gray) 6 K and (black) 12 K.
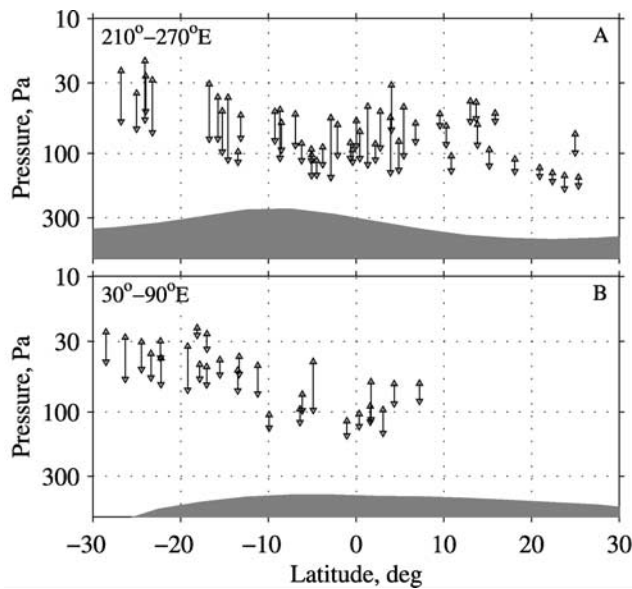
Figure 4. Distribution of elevated temperature inversions that exceed 6 K. Triangles denote the pressure at the base and peak of each inversion. Results are shown at longitudes of (a) 210°–270°E and (b) 30°–90°E. This pair of longitude bands contains half the inversions that exceed 6 K. Gray shading indicates the approximate location of the surface.

opposite side of Mars at 30°–90°E (Figure 4b), which are notably weaker than those above Tharsis, exhibit the same pattern of meridional structure.

[19] The results in Figures 3 and 4 show that the spatial distribution and vertical structure of these inversions are organized across the tropics on planetary scales. Elevated inversions appear at a wide range of locations in a pattern correlated with planetary scale topography. Although the inversions are strongest above Tharsis, they are not localized to prominent topographic features, such as the Tharsis volcanoes.

[20] Figure 5 shows longitude-height cross sections of the thermal structure in the tropics as viewed at fixed local time. This figure includes both RS measurements (Figures 5a and 5b) and an MGCM simulation (Figures 5c and 5d); the latter will be discussed in section 4.2.1. As noted previously, the RS profiles partially resolve the shallow nighttime temperature inversion near the surface, which follows the topography. The measured predawn temperature is ∼215 K at 400 Pa decreasing to ∼195 K at 200 Pa. At 6°N (Figure 5a), the most striking temperature variations appear at pressures of 50–200 Pa and longitudes of 200°–280°E, above Tharsis. This region contains a strong inversion with temperatures ranging from <165 K to >195 K. The thermal structure in subsequent measurements at 2°N is similar (Figure 5b). A moderate inversion ($\Delta T > 12$ K) also appears near 80°E in Figure 5b.

[21] In constructing Figures 5a and 5b we selected latitudes where RS profiles were obtained with nearly complete sampling in longitude (see Figure 1b). When viewed at fixed local time, the thermal structure in these figures appears to be stationary with respect to the

surface. Analogous cross sections assembled from other subsets of RS data support this conclusion.

3. Relationship of RS Results to Other Observations

[22] This section briefly discusses observations of the atmosphere by two other techniques, with emphasis on the presence or absence of elevated inversions.

3.1. Mars Pathfinder

[23] Mars Pathfinder landed on the Martian surface on 4 July 1997 at L_s = 142.7° in MY 23, one Martian year prior to the RS observations discussed in section 2. The mission included an Atmospheric Structure Investigation (ASI), which collected accelerometer measurements as the spacecraft descended through the atmosphere toward its landing site at 326.5°E, 19.1°N. Analysis of these data has yielded a profile of early morning atmospheric structure at altitudes of 9–140 km [*Schofield et al.*, 1997; *Magalhães et al.*, 1999].

[24] The ASI profile contains a strong elevated inversion, with temperature increasing from 184 K at 260 Pa to 198 K at 150 Pa. This ASI inversion has been the subject of several investigations, which suggest that it arises from radiative cooling by a water ice cloud layer [*Haberle et al.*, 1999; *Colaprete et al.*, 1999; *Colaprete and Toon*, 2000]. Although its vertical structure is reminiscent of the pronounced RS inversions that appear in Figure 2, closer comparison reveals significant differences. There is little resemblance between the ASI profile and RS profiles retrieved at essentially the same location and local time in the following Martian year. More generally, the region surrounding the Pathfinder landing site is devoid of significant RS inversions (Figure 3a). We defer further discussion of these differences to a separate paper.

3.2. MGS Thermal Emission Spectrometer

[25] No other observations of these elevated temperature inversions are currently available. The MGS Thermal Emission Spectrometer (TES) monitors the atmosphere continually, providing daily global coverage at two local times [*Smith et al.*, 2001a], but the vertical resolution of the retrieved profiles (∼10 km) is not sufficient for characterizing this type of vertical structure. Simulations conducted by B. Conrath (personal communication, 2000) support this conclusion. He began with a sample RS profile and generated synthetic infrared spectra for both the nadir and limb viewing geometries. He then used the synthetic data to test the performance of standard TES retrieval algorithms [*Conrath et al.*, 2000]. The strong inversion in the original RS profile (ΔT = 21 K) translates into a weak inversion in the TES limb retrieval (ΔT = 5 K). The response in the TES nadir retrieval is limited to changes in temperature lapse rate, but no inversion is present.

4. MGCM Simulation

[26] The RS results in section 2 provide unique insight into the nighttime thermal structure of the Martian tropics and interesting challenges for numerical models. We now
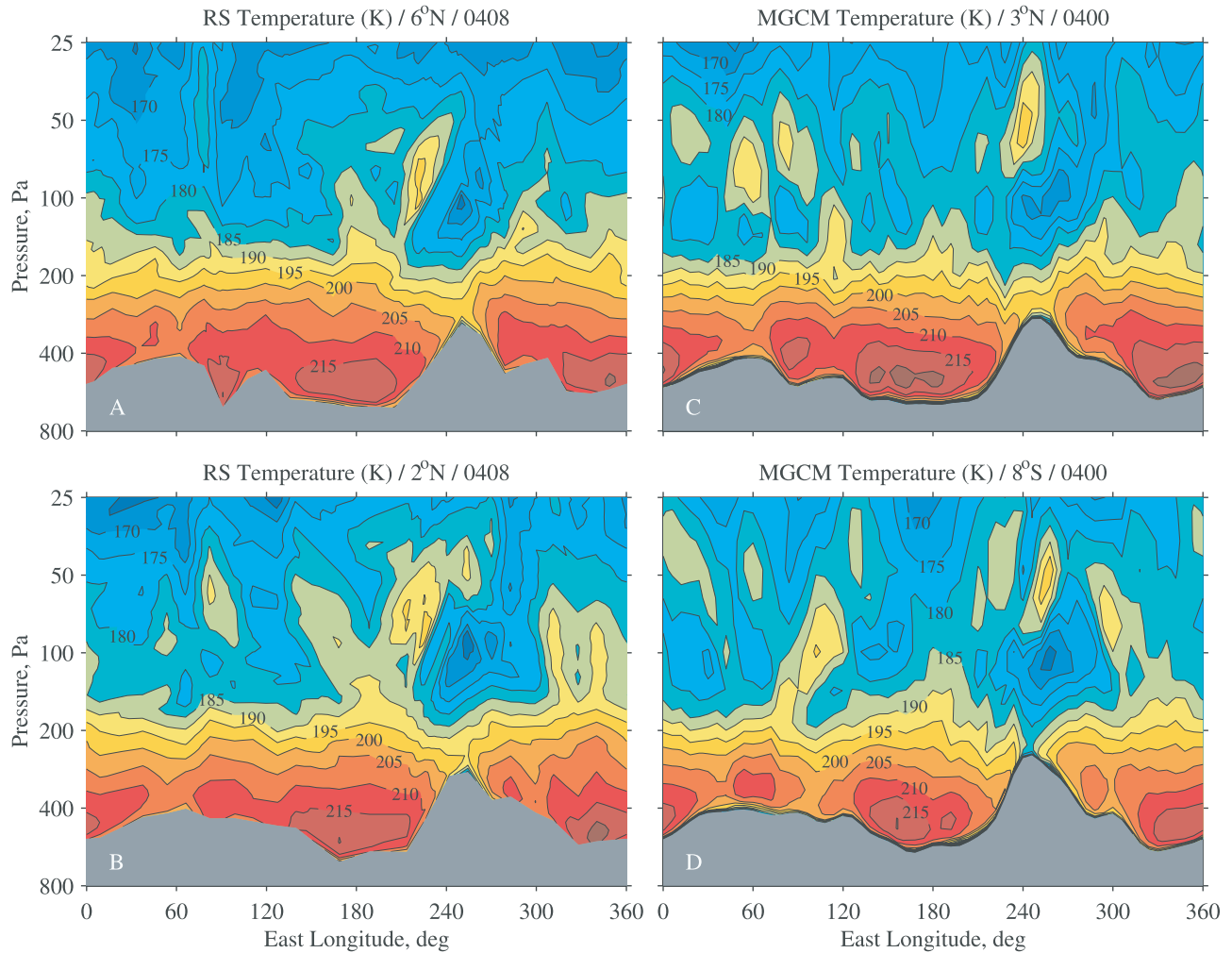
Figure 5. Thermal structure at fixed latitude and local time as it appears in (left) RS measurements and (right) MGCM simulation. Each RS cross section was constructed from a sequence of profiles spanning 25 orbits (~49 h). RS results are shown at (a) 6°N, $L_s = 145°$ and (b) 2°N, $L_s = 147°$. An analogous display of results from the MGCM simulation is shown at $L_s = 148°$ for latitudes of (c) 3°N and (d) 8°S. The local time is 0408 for the RS measurements and 0400 for the MGCM simulation. The contour interval is 5 K. Gray shading denotes the surface.

turn to the GFDL MGCM to extend our understanding of the elevated inversions beyond what can be learned from observations at fixed local time.

4.1. Model Description
4.1.1. General Characteristics
[27] The GFDL MGCM was introduced by *Wilson and Hamilton* [1996], who provide a thorough description of its initial attributes and performance. Subsequent papers trace the evolution of the model through its application to specific phenomena, such as the Hadley circulation [*Wilson, 1997; Richardson and Wilson, 2002a*], thermal tides [*Wilson, 2000, 2002*], transient eddies [*Hinson and Wilson, 2002; Wilson et al., 2002*], the water cycle [*Richardson and Wilson, 2002b*], water ice clouds [*Richardson et al., 2002*], and stationary planetary waves [*Hinson et al., 2003*].
[28] The version of the MGCM used here has been specialized to the problem at hand and it therefore differs in some respects from all previous versions. We adopt the

method for modeling atmospheric dust that was used by *Hinson et al.* [2003], but the current version has been extended to include an interactive water cycle. We model the water cycle in the same manner as *Richardson et al.* [2002], but we have added a representation of the radiative effects of water ice clouds, which were previously ignored.
[29] These simulations have a spatial resolution of 5° in latitude by 6° in longitude with 40 levels extending from the surface to an altitude of ~90 km. The results shown here are from a 5-day interval centered on $L_s = 148°$, but the model yields essentially the same results throughout the interval $L_s = 145° - 160°$.
4.1.2. Radiative Effects of Aerosols
[30] Dust and water ice clouds can influence the thermal structure of the atmosphere through absorption, scattering, and emission of radiation. We now describe the method used to model the radiative effects of these aerosols in our MGCM simulations. Their spatial distribution is discussed in section 4.1.3.
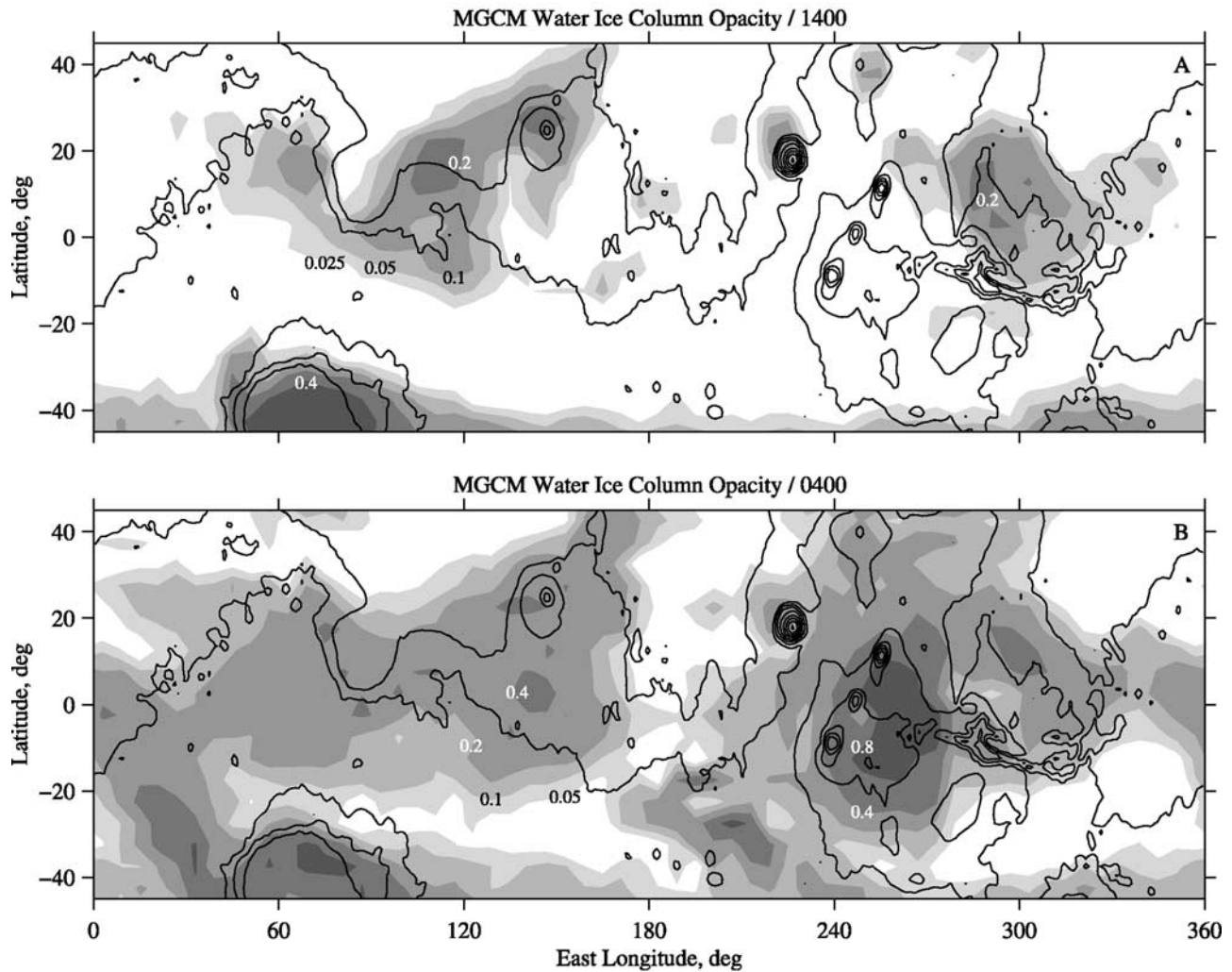
Figure 6. Distribution of water ice clouds as simulated by the MGCM at $L_s = 148°$. (a) The 12-μm column opacity at local time 1400 is indicated by gray shading at levels of 0.025, 0.05, 0.1, 0.2, and 0.4. (b) The 12-μm column opacity at local time 0400 is indicated by gray shading at levels of 0.05, 0.1, 0.2, 0.4, and 0.8. The true surface topography [*Smith et al.*, 2001] is shown by contour lines at intervals of 3 km. The topography used by the MGCM is smoother. Thermal tides are responsible for most of the variation in cloud opacity between these two local times.

[31] We use essentially the same method for modeling the radiative effects of dust as *Forget et al.* [1999]. We also include a similar representation of the radiative effects of water ice clouds, which are often ignored [e.g., *Forget et al.*, 1999; *Richardson et al.*, 2002]. Although generally secondary to dust in their influence on thermal structure, water ice clouds are efficient emitters of thermal radiation, and the resulting radiative cooling can be significant when the cloud infrared opacity exceeds ∼0.1 [*Haberle et al.*, 1999; *Colaprete and Toon*, 2000]. Through this mechanism nighttime clouds play a prominent role in the simulations presented here.

[32] Three parameters characterize the radiative properties of the aerosols: the single scattering albedo ω, the asymmetry parameter g, and the extinction cross section efficiency Q_{ext}. In the interest of computational speed the current version of the MGCM considers only Planck-weighted averages of these scattering parameters within selected wavelength bands.

[33] We represent the Sun as a black-body source at a temperature of 6000 K, and we model the interaction of solar radiation with atmospheric aerosols using a single band (0.1–5 μm). The radiative transfer calculations are simplified through use of the two-stream delta-Eddington approximation, appropriate when the scattering phase function has a strong peak in the forward direction. In the simulations described here, water ice clouds have a minor impact at visible wavelengths. This is due in part to the patchy coverage and weak opacity of the simulated daytime clouds (see Figure 6a). In addition, the cloud influence is dominated by scattering ($\omega = 0.98$ in the visible) so that absorption is weak.

[34] We use three wavelength bands to represent radiative transfer in the thermal infrared. As in previous models, one band spans 11.6–20 μm [e.g., *Pollack et al.*, 1990; *Forget et al.*, 1999], including the prominent CO_2 absorption feature near 15 μm. Within this band, we ignore scattering and treat the aerosols as gray absorbers,

Table 1. Radiative Properties of Aerosols Adopted for MGCM Calculations

Band (Wavelength)	Dust[a]	Water Ice[b]
Solar (0.1–5 μm)	Q_{ext} = 2.5	Q_{ext} = 2.5
	ω = 0.92	ω = 0.98
	g = 0.75	g = 0.80
Infrared (5–11.6 μm)	Q_{ext} = 1.346	Q_{ext} = 1.313
	ω = 0.480	ω = 0.484
	g = 0.501	g = 0.809
Infrared (11.6–20 μm)[c]	Q_{ext} = 0.749	Q_{ext} = 1.691
	ω = 0.356	ω = 0.516
	g = 0.521	g = 0.619
	Q_{abs} = 0.482	Q_{abs} = 0.818
Infrared (20–100 μm)	Q_{ext} = 0.419	Q_{ext} = 0.372
	ω = 0.316	ω = 0.437
	g = 0.362	g = 0.337
9 μm	Q_{abs} = 1.160	
12 μm		Q_{abs} = 1.315

[a]Values are for a modified gamma size distribution, with r_{eff} = 1.5 μm and v_{eff} = 0.4, at a temperature of 215 K.
[b]Values are for spherical particles of radius 4 μm at a temperature of 180 K.
[c]Scattering by aerosols is ignored within this band.

as discussed by *Forget et al.* [1999]. The absorption efficiency $Q_{abs} \equiv (1 - \omega) \, Q_{ext}$.

[35] The remaining two infrared bands cover shorter (5–11.6 μm) and longer (20–100 μm) wavelengths. This is the same approach used by *Forget et al.* [1999], while *Pollack et al.* [1990] merged these two intervals into one composite band. Within each interval, the MGCM uses a two-stream algorithm [*Toon et al.*, 1989] to calculate the effects of absorption and scattering by aerosols. It relies on the hemispheric mean approximation and represents Planck emission with a source function method.

[36] Table 1 lists the values for Q_{ext}, ω, and g that were used in this simulation. Parameter values for dust correspond to a modified gamma size distribution with r_{eff} = 1.5 μm and v_{eff} = 0.4 [*Wolff and Clancy*, 2003] at a temperature of 215 K. Parameter values for water ice are based on Mie calculations for spherical particles (pure ice) at a temperature of 180 K. For simplicity, we assume that the ice particles are uniform in size with a radius of 4 μm. This value is consistent with recent observations [e.g., *Pearl et al.*, 2001; *Clancy et al.*, 2003; *Wolff and Clancy*, 2003; *Glenar et al.*, 2003].

[37] Cloud formation most likely involves heterogeneous nucleation of ice onto dust particles, but this version of the MGCM does not include an explicit treatment of the interaction between the two types of aerosol. However, the model mimics the effect of condensing water ice by replacing the scattering parameters for dust with those appropriate to water ice when the cloud opacity exceeds the dust opacity within a given vertical layer. For example, ω would increase from 0.92 to 0.98 in the solar band, which represents the brightening of the aerosol as a larger proportion of the dust particles becomes coated with water ice.

4.1.3. Distribution of Aerosols

[38] The spatial distribution of dust is prescribed and remains fixed, with no variations in response to sedimentation, eddy mixing, or advection. This approach is motivated by our interest in the radiative effects of water ice clouds, which are more easily assessed when the distribution of dust

is controlled in this way (see section 4.2.3). Our model for the spatial distribution of dust resembles the one used by *Forget et al.* [1999]. The reference mixing ratio is horizontally uniform but dust is mixed to higher altitudes in the tropics than at the poles.

[39] This model for the dust distribution can be tuned by scaling the column opacity at a reference location. We selected a value by comparing the simulated thermal structure with the RS measurements (e.g., Figure 5) and with the zonal mean temperature field observed simultaneously by TES [e.g., *Smith et al.*, 2001a]. Near $L_s = 150°$ we find good overall agreement between the simulation and these measurements when the dust visible opacity is 0.3 in the tropics. This value for the visible opacity is also consistent with TES observations in the infrared. *Smith et al.* [2001b] report a column opacity at 9 μm of ~0.15 in the tropics at this season, while *Clancy et al.* [2003] conclude that the dust opacity is ~2 times larger in the visible than at 9 μm.

[40] We adopt the simple model for water ice clouds that was used previously by *Richardson et al.* [2002]. The model accounts for cloud microphysical effects by imposing instantaneous phase changes between water vapor and ice at each model time step. All supersaturated water vapor is converted immediately to cloud ice. Conversely, cloud ice sublimates immediately whenever the local vapor pressure falls below saturation. The spatial distribution of ice particles evolves in response to both advection and sedimentation.

[41] Our MGCM simulations using this simple cloud model overestimate the total cloud mass, though not by as large a factor as in a previous investigation [*Richardson et al.*, 2002]. This improvement appears to result from an increase in vertical resolution along with refinements in the calculations of radiative transfer. *Richardson et al.* [2002] reduced the cloud mass to a more plausible level by enhancing the sedimentation rate of the water ice particles. The approach used here is somewhat different. We retain the sedimentation rate appropriate to particles with a radius of 4 μm, but we scale the cloud opacity by a constant factor, which remains fixed throughout the simulation. All results shown here are from simulations in which the cloud opacity has been reduced by 50%. This value was selected to constrain the radiative effects of the simulated clouds to a level consistent with available observations. Without such scaling the simulated clouds would produce overly strong radiative cooling, particularly at night. The spatial distribution of the clouds is insensitive to this change in opacity.

[42] Figure 6a shows a map of the 12-μm column opacity of water ice clouds at local time 1400 as simulated by the MGCM. The model produces a cloud belt in the northern tropics as well as polar hood clouds at high latitudes in the south. The zonal average of opacity in the northern tropics is ~0.05, consistent with TES observations at this season [*Pearl et al.*, 2001, Plate 1; *Smith et al.*, 2001b; *Smith*, 2004]. Notable enhancements of cloud opacity (0.1–0.2) appear in the tropics above Olympus Mons, Alba Patera, Lunae Planum, Syrtis Major, Elysium Mons, and east of Isidis Planitia.

[43] The results in Figure 6a are generally consistent with the distribution of water ice clouds observed at the same local time by TES [*Smith*, 2004, Figure 16; *Pearl et al.*, 2001, Plate 2] and by the MGS Mars Orbiter Camera
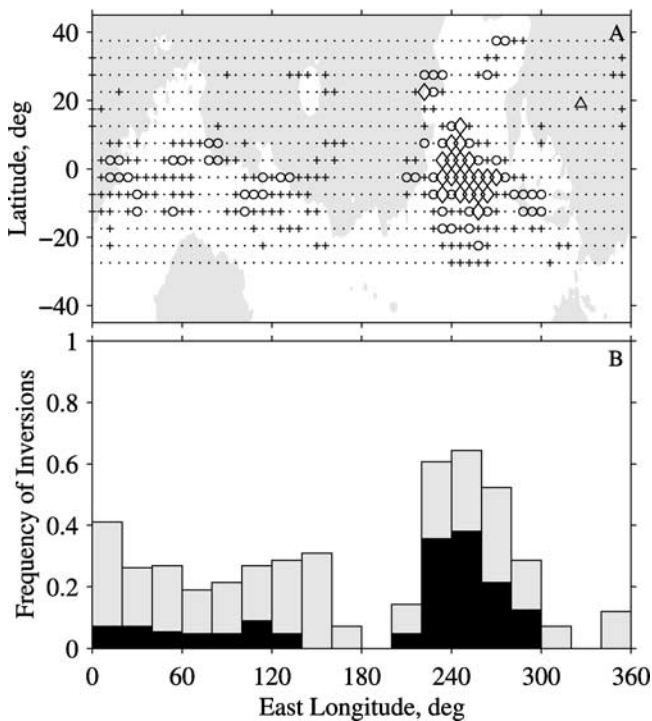
Figure 7. (a) Distribution of tropical temperature inversions at local time 0400 as simulated by the MGCM. Symbols show locations where profiles contain significant elevated inversions, using the same notation as in Figure 3. A triangle shows the Mars Pathfinder landing site. Shading denotes negative surface elevation. (b) A histogram showing the fraction of simulated profiles that contains an inversion larger than (gray) 6 K and (black) 12 K.

(MOC) [e.g., *Liu et al.*, 2003, Figure 19]. The most significant discrepancy is that the localized afternoon clouds observed by TES and MOC above Ascraeus, Pavonis, and Arsia Mons are absent from Figure 6a. This is a consequence of the 5° by 6° grid spacing used in this simulation, which fails to resolve these dramatic topographic features. The simulation of these localized orographic clouds improves when the MGCM is run at finer resolution (2° by 2.4°).

[44] With this approach to cloud modeling, the MGCM achieves a reasonably accurate simulation of the daytime tropical water ice cloud belt. Its opacity was decreasing during the span of the RS experiments considered here in response to a seasonal increase in temperature [*Smith et al.*, 2001b; *Wang and Ingersoll*, 2002; *Liu et al.*, 2003; *Smith*, 2004]. However, the column abundance of water vapor in the tropics remained substantial (∼20 pr-µm) during this interval [*Smith*, 2002].

[45] This simulation is characterized by strong diurnal variation in the properties of tropical water ice clouds, as illustrated in Figure 6b. At local time 0400 the simulated clouds have a larger opacity and broader spatial coverage than at 1400. The nighttime opacity is largest (0.4−1) in the Tharsis region, and the zonal mean opacity is ∼0.25 throughout the tropics at 0400. No direct observations are available at this local time (see section 5). As we will

show in section 4.2.2, these prominent nighttime clouds form in response to wave-induced adiabatic cooling.

4.2. MGCM Results
4.2.1. Thermal Structure

[46] Figures 5c and 5d show longitude-height cross sections of the simulated thermal structure at latitudes of 3°N and 8°S. The average temperature is ∼215 K at 400 Pa and ∼195 K at 200 Pa, in good agreement with the RS measurements in Figures 5a and 5b. The strong inversion in the simulation at longitudes of 220°−270°E resembles the thermal structure observed above Tharsis, with temperature extremes at 8°S of >195 K at 50 Pa and <165 K at 100 Pa. Less dramatic inversions appear in the simulation at other longitudes, such as at 80°E in Figure 5c and at 110°E in Figure 5d, reminiscent of the wide distribution of moderate inversions in the observations (Figure 3). Note also the similarity at longitudes of 40°−100°E between the moderate temperature inversions in the measurements (Figure 5b, 2°N) and the simulation (Figure 5c, 3°N).

[47] We characterized the strength and spatial distribution of elevated inversions in the simulated temperature field using the method described previously in section 2.2. The results appear in Figure 7. The simulation is similar to the measurements in many respects: (1) the inversions are strongest and occur most frequently above elevated terrain; (2) the strongest inversions ($\Delta T > 18$ K) are restricted to longitudes of 220°−270°E, above Tharsis; (3) moderate inversions ($\Delta T = 12-18$ K) appear sporadically above the elevated terrain north of Hellas at 10°N−15°S, 0°−140°E; (4) few significant inversions are present above the low-lying planitia of the northern tropics, and none occur in the vicinity of the Pathfinder landing site; and (5) significant inversions are scarce at longitudes of 160°−200°E. There are notable differences as well, such as near 25°N, 228°E (north of Olympus Mons) where the simulated inversions are stronger than those observed. Nevertheless, the many similarities between the simulation and the observations, both here and in Figure 5, suggest that the quality of the simulation is sufficient to provide valuable insight into the RS measurements.

[48] We will show later in this section that the simulated inversions are caused by thermal tides. Before proceeding, it is useful to interject a brief review of basic concepts and notation. The zonal and temporal structure of thermal tides can be expressed as

$$T(\lambda, t_L) = \sum A_{s,\sigma} \cos\left[(s - \sigma)\lambda + \sigma \Omega t_L - \delta_{s,\sigma}\right], \qquad (1)$$

where T is temperature, λ is east longitude, t_L is the local true solar time, s is the zonal wave number (0, ±1, ±2, . . .), Ω is the rotation rate of Mars, and σ is a positive integer that determines the frequency. Both s and σ are dimensionless. This expression can be converted to universal time t_U by noting that $\Omega t_L = \Omega t_U + \lambda$. The summation in (1) includes contributions from a variety of "modes" with amplitude $A_{s,\sigma}$ and phase $\delta_{s,\sigma}$. We will use the notation $T_{s,\sigma}$ to refer to a single term in this summation. (A more fundamental description of the tides involves eigenfunctions of Laplace's tidal equation, and there is a distinct set of such Hough functions associated with each choice for s and σ [e.g., *Andrews et al.*, 1987, section 4.2].)
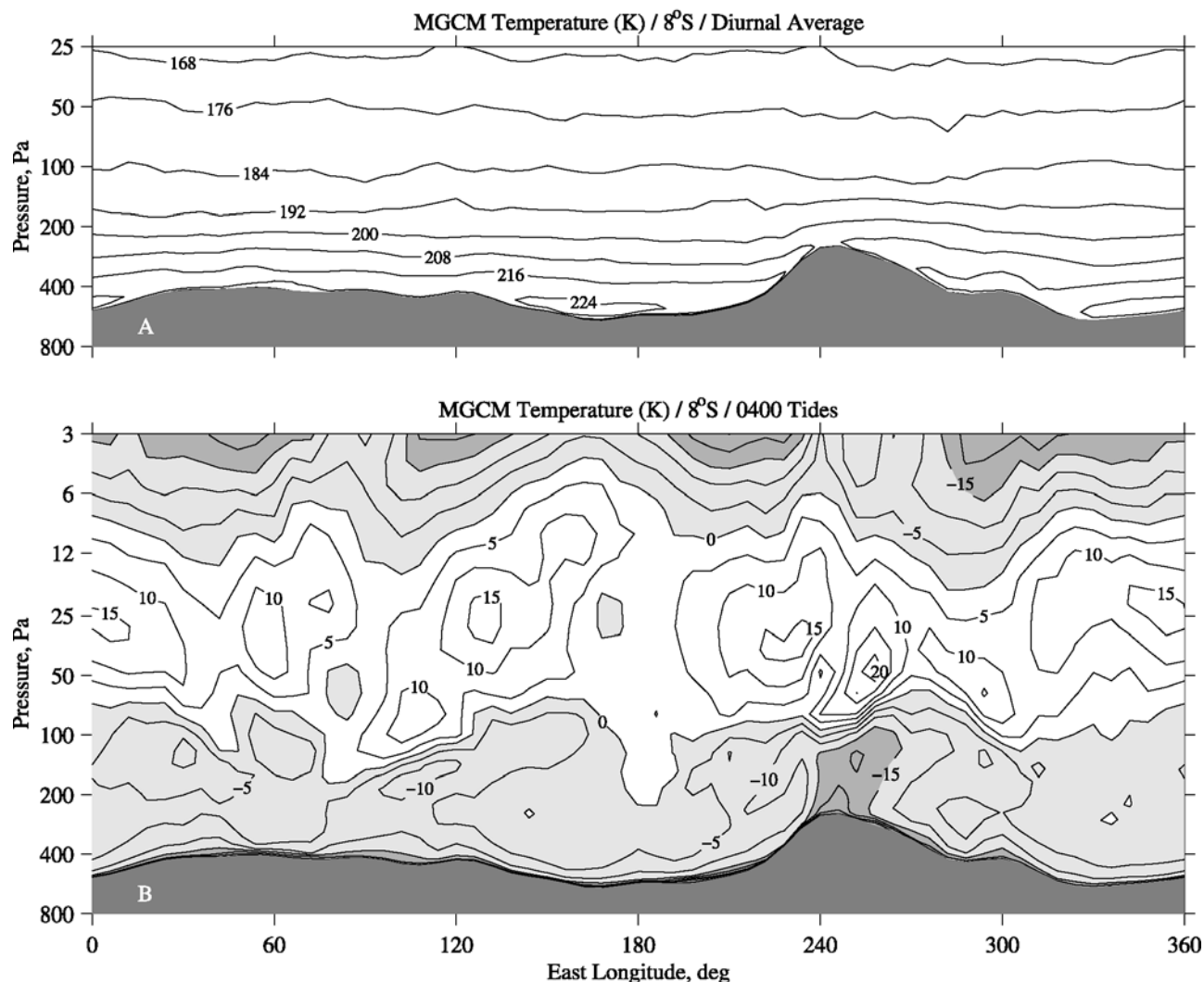
Figure 8. Cross sections of thermal structure at 8°S as simulated by the MGCM. (a) The diurnal average. The contour interval is 8 K. Dark shading denotes the surface. (b) The perturbation due to thermal tides at 0400. The contour interval is 5 K, and light shading indicates negative values. The lower panel has been extended upward to better illustrate the vertical structure of the tides. The temperature field in Figure 5d is the sum of (a) and (b).

[49] Thermal tides fall into two categories, and both types are subject to aliasing in these RS observations [cf. *Banfield et al.*, 2003]. Solar-locked tides are forced directly by solar heating and move with the Sun ($s = \sigma$). They exhibit no variation with longitude when observed at fixed local time. In addition, modulation of the solar-locked tides by topography and surface thermal properties excites solar-asynchronous tides ($s \neq \sigma$) that do not follow the Sun's apparent motion [*Zurek*, 1976; *Zurek et al.*, 1992]. These can propagate westward at different phase speeds than the solar-locked tides ($s > 0$, $s \neq \sigma$), eastward ($s < 0$), or not at all ($s = 0$). When viewed at fixed local time, the solar-asynchronous tides appear as zonally varying disturbances with wave number $|s - \sigma| > 0$.

[50] With this background, we now return to the simulation. Figure 8 provides a different perspective on the simulated thermal structure at 8°S (Figure 5d). The temperature field in Figure 8a has been averaged over local time to remove the first-order effects of thermal tides. The temperature decreases steadily with increasing height, except very close to the surface, and there is no sign of an appreciable elevated inversion. At pressures >150 Pa, the isotherms include zonal modulation that tends to follow the surface topography.

[51] Figure 8b shows the temperature deviations caused by thermal tides at 0400, as obtained by subtracting the diurnal average from the 0400 temperature field. Solar-locked tides contribute the component that is independent of longitude, as reflected in the dark and light bands that alternate vertically. This zonal mean component is predominantly diurnal with a vertical wavelength of ~35 km and a phase at this local time that results in a temperature maximum near the 30-Pa pressure level [cf. *Wilson and Richardson*, 2000]. The zonal variations arise from solar-asynchronous tides. These, too, are primarily diurnal, although semidiurnal modes contribute appreciably at some
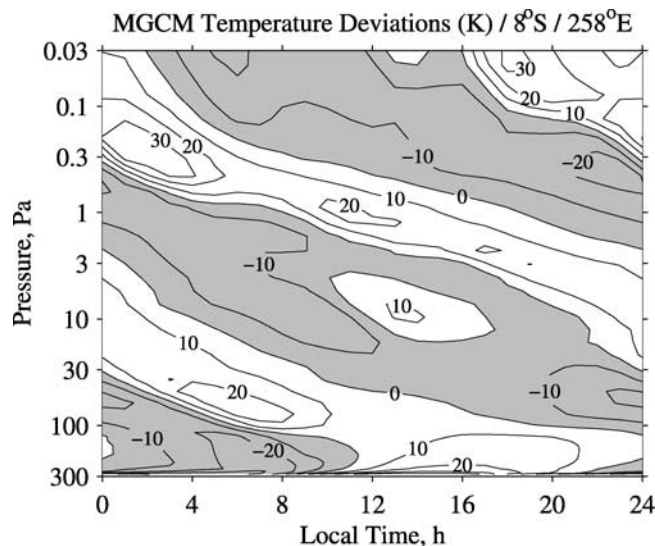
Figure 9. Temperature deviations at 8°S, 258°E and their variation with local time as simulated by the MGCM. The contour interval is 10 K and gray shading denotes negative values. This pressure range extends from the surface to an altitude of ~80 km.

locations. The net temperature deviations are strongest at 220°–270°E, where the amplitude reaches +25 K at 50 Pa (258°E) and −21 K near 125 Pa (252°E).

[52] Figure 9 takes a closer look at the time evolution of temperature deviations at a fixed location above Tharsis (8°S, 258°E). The downward progression of these temperature deviations reflects the downward phase propagation of tides within the tropics [cf. *Wilson and Richardson*, 2000, Figure 12]. It is apparent from Figure 9 that the tides at this location are primarily diurnal, although the semidiurnal tides are appreciable at all pressures and are most noticeable near 10 Pa.

[53] Figures 8 and 9 demonstrate that thermal tides are responsible for the simulated temperature inversions, producing elevated inversions that descend steadily with increasing local time. The inversions coincide with longitudes of enhanced tidal amplitude, with the strongest enhancement occurring above Tharsis, which is evidently a major source of excitation for the solar-asynchronous tides.

[54] Figure 10 illustrates the effect of the tides on temperature profiles above Tharsis (8°S, 258°E). The figure is restricted to the pressure range sounded by the RS experiments, although significant variations occur at higher altitudes (see Figure 9). The temperature near the base of the profiles varies widely with local time in response to daytime solar heating and nighttime radiative cooling of the surface, as expected. A strong elevated inversion is present at local times of 0100, 0400, and 0700 (Figure 10a). The inversion descends steadily with increasing local time in response to the downward phase propagation of the tides. At 0400 the simulated inversion is characterized by temperature extremes of 163 K at 100 Pa and 200 K at 50 Pa. This profile closely resembles the vertical structure observed at the same longitude and local time in Figures 2b and 2c.

[55] By local time 1000 the simulated inversion has largely vanished, and Figure 10b shows that temperature variations within this pressure range during the remainder of the day are less dramatic than in the early hours. There is relatively little variation among the simulated profiles at 1300, 1600, and 1900 (Figure 10b), except very close to the surface. The diurnal cycle is completed as an elevated inversion descends into the pressure range sounded by the RS experiments at 2200 (see Figure 9).

[56] Figure 11 shows a latitude-height cross section of the simulated thermal structure at 258°E, including both the diurnal average (Figure 11a) and the perturbation due to thermal tides at 0400 (Figure 11b). The strong meridional temperature gradient at middle to high southern latitudes in Figure 11a is characteristic of the basic seasonal state of the atmosphere [cf. *Smith et al.*, 2001a, Plate 5; *Haberle et al.*, 1999, Figure 4; *Hinson and Wilson*, 2002, Figure 1]. As was the case in Figure 8a, no significant elevated inversion is present in the diurnally averaged temperature field.

[57] The spatial structure of the simulated thermal tides in Figure 11b is asymmetric about the equator, with two important consequences. First, the tidal amplitude is larger in the southern tropics than in the north, resulting in a southward bias in the distribution of elevated inversions. Within the region accessible to RS measurements, the tidal amplitude at 258°E is sufficient to produce inversions only at latitudes south of ~10°N. Second, contours of tidal amplitude in the southern hemisphere slope upward with increasing distance from the equator, so that the height of the inversions increases steadily toward the south. The simulated thermal structure resembles the RS observations in both respects (see Figures 2–4).

[58] The north-south asymmetry of the tides in Figure 11b probably arises from two sources. First, the tides respond to variations in surface topography, as noted previously in connection with Figures 3 and 7, and the topography is distinctly asymmetric about the equator (see Figure 1a). Second, the meridional structure of the tides is also influenced by the mean zonal wind field, which is highly asymmetric at this season. A strong eastward jet, with winds exceeding 100 m s^{-1}, appears at high latitudes in
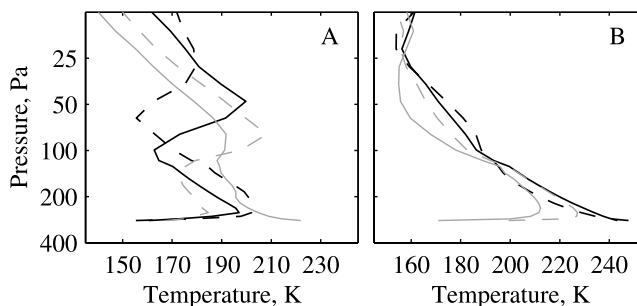
Figure 10. The diurnal cycle of thermal structure as simulated by the MGCM at 8°S, 258°E. The profiles in (a) are at local times of (dashed black) 0100, (solid black) 0400, (dashed gray) 0700, and (solid gray) 1000. The profiles in (b) are at local times of (dashed black) 1300, (solid black) 1600, (dashed gray) 1900, and (solid gray) 2200. All profiles extend to within ~100 m of the surface, where the pressure is ~290 Pa.
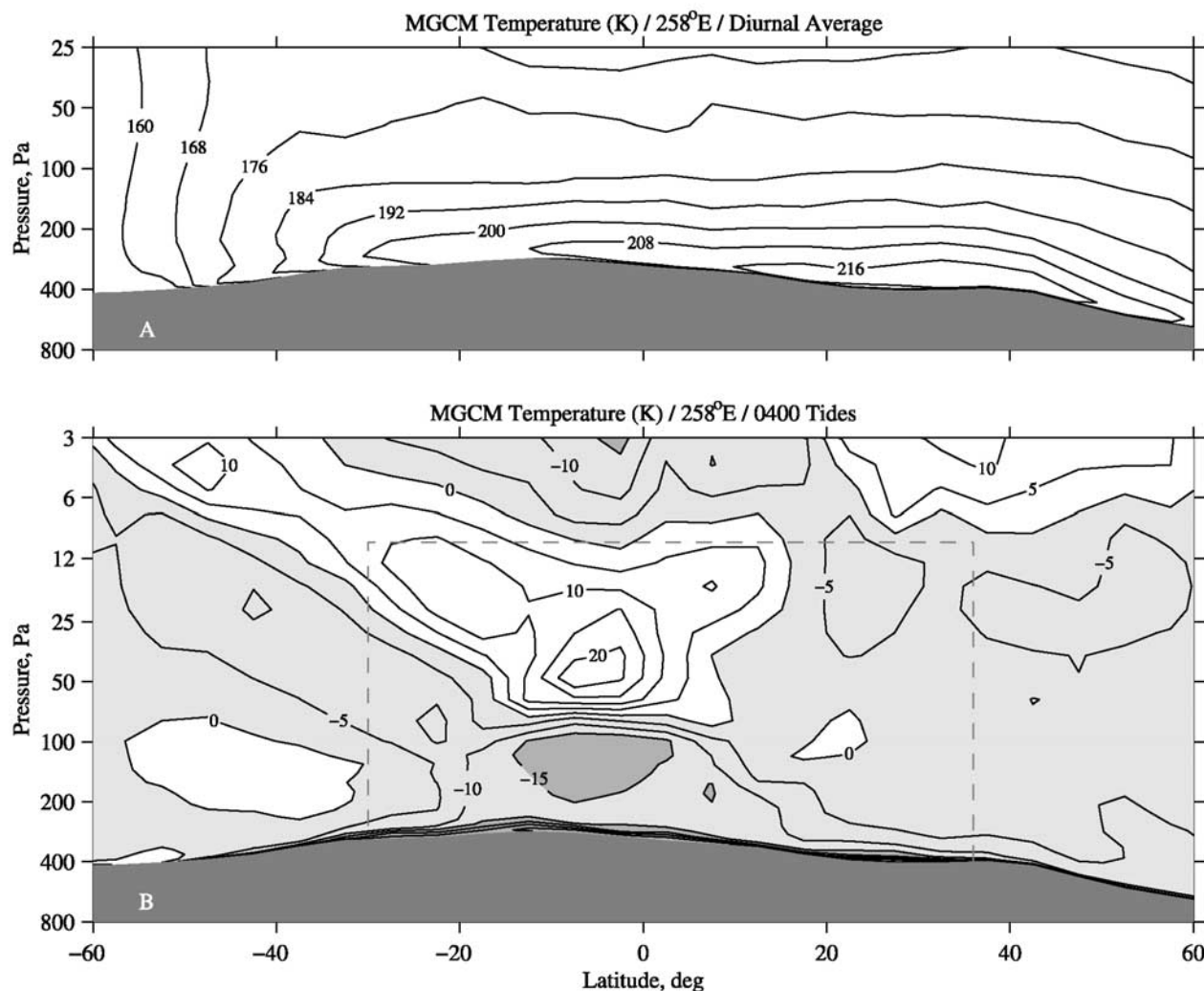
Figure 11. Cross sections of thermal structure at 258°E as simulated by the MGCM. (a) The diurnal average. The contour interval is 8 K. Dark shading denotes the surface. (b) The perturbation due to thermal tides at 0400. The contour interval is 5 K, and light shading indicates negative values. The lower panel has been extended upward to better illustrate the vertical structure of the tides. The dashed line bounds the region sounded by RS experiments.

the south, while the zonal winds in the north are comparatively weak [e.g., *Smith et al.*, 2001a, Plate 5; *Haberle et al.*, 1999, Figure 4; *Hinson and Wilson*, 2002, Figure 1].

[59] In summary, we compared the simulated and observed temperature fields, with emphasis on the conspicuous elevated inversions, and we find strong similarities. These simulated inversions arise from thermal tides, and we conclude that tides are also responsible for the corresponding inversions in the RS observations.
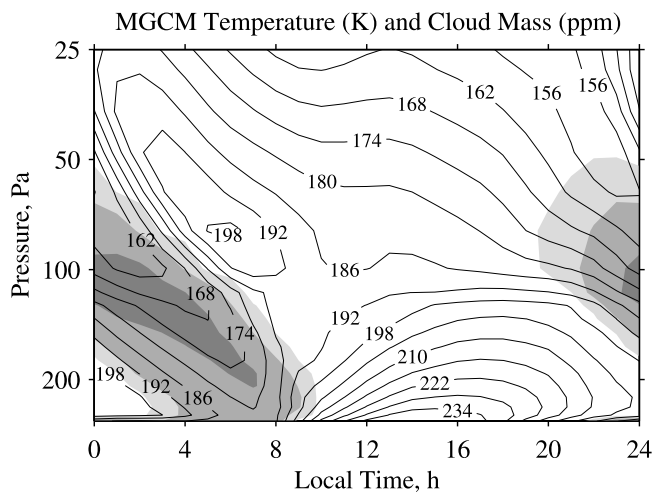
4.2.2. Water Ice Clouds

[60] We now turn our attention to water ice clouds in order to illustrate their distinctive spatial and temporal structure, their radiative effects, which are considerable, and their interaction with the tides.

[61] Figure 12 shows the structure of the simulated clouds and its evolution with local time at 8°S, 252°E. The thermal structure at this location includes a strong elevated inversion similar to the one described previously in Figure 10. A prominent cloud layer forms at night, and its structure and time variation are closely coupled with the inversion. A decrease in temperature near the 80-Pa pressure level initiates cloud formation at a local time of ~2000. During the remainder of the night, the cloud layer resides near the temperature minimum at the base of the elevated inversion, and both the inversion and the cloud layer descend steadily with increasing local time. The cloud dissipates after 0700 in response to wave-induced adiabatic warming and direct solar heating. The column opacity of the cloud at 12 μm is substantial at night (~1), but the sky becomes clear at this location during the day.

[62] Figure 13 shows a cross section of the simulated cloud structure at the same latitude (3°N) and local time (0400) as the thermal structure in Figure 5c. Clouds appear within a relatively narrow layer (100–200 Pa at 0400) at a variety of longitudes. This entire cloud layer evolves with local time in the manner described in Figure 12. The cloud structure is closely coupled to the thermal structure, with a direct correspondence between temperature minima that

Figure 12. Characteristics of simulated water ice clouds at 8°S, 252°E and their variation with local time. The water ice mass mixing ratio is indicated by gray shading at levels of 25, 100, and 225 parts per million. This is superimposed on a contour plot of temperature, with a contour interval of 6 K.

appear below elevated inversions (Figure 5c) and enhancements in water ice mixing ratio (Figure 13). The densest cloud appears above Tharsis in connection with the strongest temperature inversion. Note that ground fog also forms adjacent to the surface in the Tharsis region, where the surface thermal inertia is relatively low.

[63] According to our MGCM calculations, the cooling rate due to thermal emission from the cloud in Figure 12 reaches ~100 K sol^{-1} at local times of about 2300–0700. (This is comparable to the nighttime cooling rate produced by ground fogs in the simulations of *Colaprete and Toon* [2000].) The cooling rates associated with less prominent clouds, such as those at 40°–100°E in Figure 13, are smaller in magnitude but still sufficient to influence the thermal structure in the tropics. This radiative forcing has the same distinctive spatial and temporal structure as the clouds, which results in strong coupling between tropical tides and water ice clouds in our simulation.

[64] The nature of this radiative-dynamical coupling can be summarized as follows. Wave-induced adiabatic cooling initiates cloud formation at specific locations and local times, and prominent clouds occupy the temperature minima at the base of elevated inversions. In this way the tides strongly influence the structure and evolution of the water ice clouds, as illustrated in Figures 12 and 13. The radiative cooling produced by these clouds is therefore highly correlated with the thermal structure of the tides. This radiative forcing results in strong positive feedback that amplifies the tides and enhances the elevated inversions.

[65] The MGCM simulation indicates that the nighttime temperature minimum at the base of the elevated inversion in Figure 12 results from a combination of dynamical (adiabatic) and radiative cooling, while the nighttime temperature maximum at the peak of the inversion results entirely from adiabatic warming by the tides. In this regard, Figure 12 illustrates the extent to which the tides control the clouds. At the 100-Pa pressure level, the temperature

increases from ~162 K at 0300 to ~192 K at 0600. This warming arises from tidal dynamics and completely overwhelms the radiative cooling effect of the cloud, which is substantial. Tides drive the cloud to progressively lower altitudes.

4.2.3. Simulation With Passive Clouds

[66] We conducted a supplementary simulation with the MGCM to illustrate the fundamental connection between the inversions and tides. This experiment differs from our baseline simulation only in that the radiative effects of water ice clouds are ignored. Figure 14a shows the temperature deviations caused by thermal tides at 8°S, 0400 in the absence of cloud radiation. This should be compared with Figure 8b, which shows the corresponding result from the simulation with radiatively active clouds. Both simulations yield similar spatial patterns of temperature deviations, but cloud radiation intensifies both the solar-locked and solar-asynchronous components of the tides in Figure 8b. This amplification of the tides results not only in colder temperatures where radiative cooling occurs (100–200 Pa at 0400) but also in dynamical warming at higher altitudes (10–60 Pa at 0400). The magnitude of these changes is large, exceeding 10 K at some locations. This combination of cooling at the base and warming at the peak produces much stronger inversions. The simulation that includes radiatively active clouds agrees more closely with the RS measurements.

[67] Figure 14 illustrates other properties of the tides in the simulation that ignores cloud radiation. The solar-asynchronous tides cause substantial zonal variations of temperature even in this simulation. Their effect is most pronounced at high altitudes, particularly at local time 1600 (Figure 14b). The phase of the tides at 1600 produces elevated temperature inversions at pressures of 5–10 Pa. These appear not only above Tharsis but also at other longitudes, such as near 320°E and in the opposite hemisphere near 60°E. In the absence of positive feedback from cloud radiation, these inversions weaken as they descend
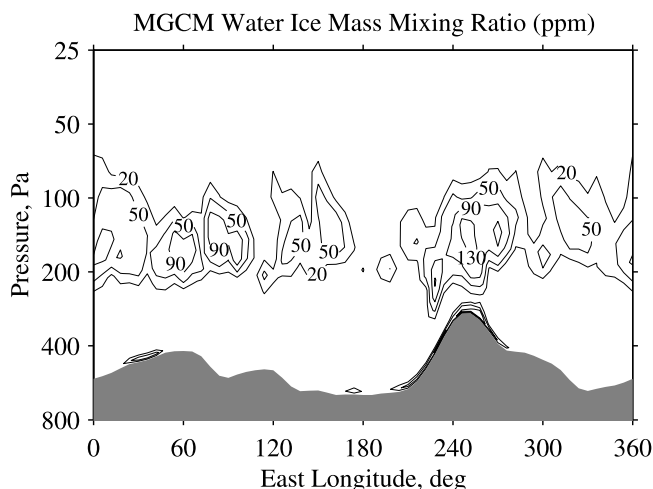
Figure 13. Cross section of water ice mass mixing ratio as simulated by the MGCM at 3°N, 0400. The contour levels are 20, 50, 90, and 130 parts per million. Gray shading denotes the surface.
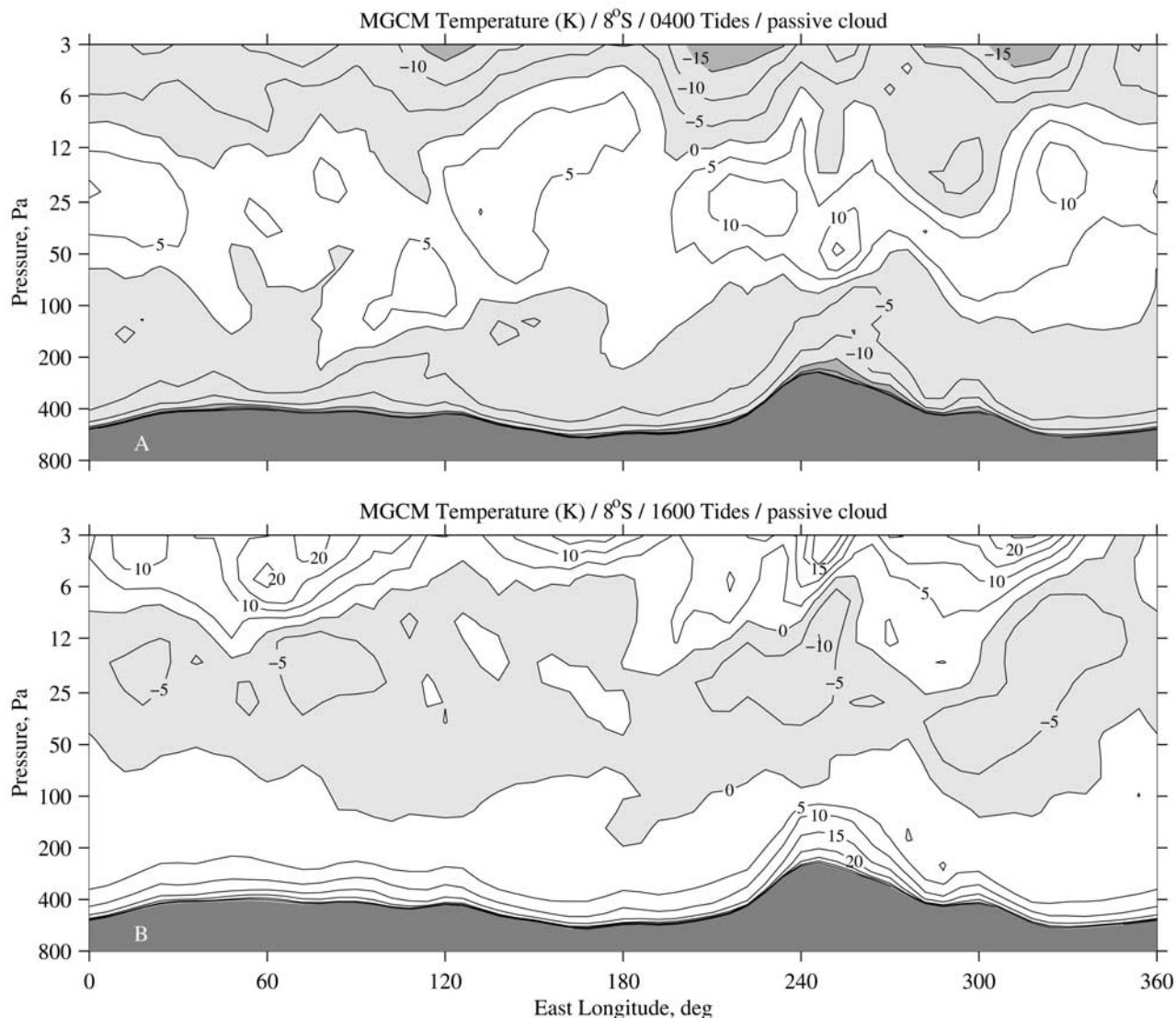
Figure 14. Temperature perturbations caused by thermal tides in a simulation where the radiative effects of water ice clouds are ignored. Results are shown at the same latitude (8°S) as in Figure 8b for local times of (a) 0400 and (b) 1600. The contour interval is 5 K. Light shading indicates negative values, while dark shading denotes the surface.

with increasing local time, resulting in modest inversions at pressures of 50–100 Pa at 0400.

[68] Finally, Figure 15 shows a latitude-height cross section of tidal temperature deviations from the simulation with passive clouds. The corresponding result from the simulation with radiatively active clouds appears in Figure 11b. Comparison of these two figures shows once again that cloud radiation intensifies the tides but that the spatial structure of the tides is essentially the same in both cases. The results in Figures 14 and 15 imply that tides control the basic behavior of the elevated inversions, with clouds providing strong amplification through nighttime radiative cooling.

5. Discussion

[69] Space-time spectral analysis of the simulated temperature field reveals that a large number of tidal modes

contribute to the formation of elevated inversions. These modes interfere constructively at some longitudes, particularly above Tharsis, and destructively at others. This zonal interference pattern reflects the basic topographic forcing that excites the solar-asynchronous tides. Not surprisingly, Tharsis plays a dominant role in this process.

[70] The westward propagating diurnal modes are an essential component of the simulated inversions. For example, both the $T_{3,1}$ and $T_{4,1}$ modes have amplitudes of $\sim$2 K and vertical wavelengths of $\sim$20 km near the equator. The eastward propagating diurnal modes, such as $T_{-1,1}$ and $T_{-2,1}$, have larger vertical wavelengths but still play an important role in shaping the structure of the inversions. The zonally symmetric mode $T_{0,1}$ also makes a notable contribution.

[71] The westward diurnal modes, $T_{3,1}$ and $T_{4,1}$, are planetary scale gravity waves, while the eastward diurnal
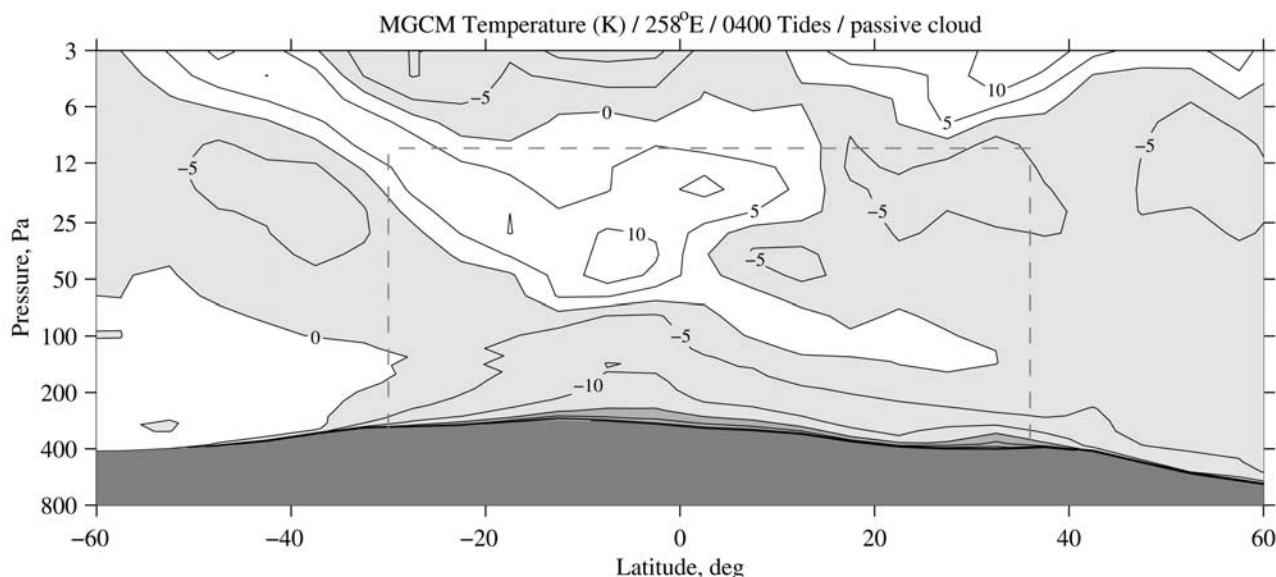
Figure 15. Temperature perturbations caused by thermal tides in a simulation where the radiative effects of water ice clouds are ignored. Results are shown at the same longitude (258°E) and local time (0400) as in Figure 11b. The contour interval is 5 K. Light shading indicates negative values, while dark shading denotes the surface. The dashed line bounds the region sounded by RS experiments.

modes, $T_{-1,1}$ and $T_{-2,1}$, include a strong contribution from diurnal-period Kelvin waves (also known as DK1 and DK2, respectively). The interference among these diurnal modes was illustrated in previous simulations of tropical tides with the GFDL MGCM [*Wilson*, 2000, Figure 3; *Wilson et al.*, 2003, Figure 4]. Among these modes only the ones with relatively large vertical wavelengths, such as DK1 and DK2, are resolved by TES [*Wilson*, 2000; *Banfield et al.*, 2003].

[72] Prominent nighttime clouds form within an elevated layer above Tharsis in our simulation (Figures 6b, 12, and 13). They descend steadily through the night, merge with the ground fog after 0400, diminish after 0700 in response to a combination of adiabatic warming and direct solar heating, and vanish by 1000. In this regard the simulation is qualitatively consistent with the properties of early morning clouds observed above Tharsis during the northern summer season. For example, an image from the Hubble Space Telescope (HST) at $L_s = 94°$ (16 June 1993, MY 21) contains bright water ice clouds in the region surrounding the three Tharsis volcanoes and Olympus Mons [*Clancy et al.*, 1996, Figure 16], reminiscent of the simulated cloud structure (Figure 6b). The peaks of the volcanoes are visible above the cloud deck in this HST image, reflecting the confinement of the clouds to low altitudes (<10 km) at the local time of this observation (~0900). *Akabane et al.* [2002] have tracked the diurnal variation of this so-called "Tharsis morning cloud" during early northern summer. In observations near $L_s = 116°$ (18–24 April 1982, MY 15), its opacity decreased steadily during the morning from ~1.2 at 0730 to ~0.2 at 1130. A similar pattern of diurnal variation was observed in other years [*Akabane et al.*, 2002].

[73] Nighttime clouds such as those that appear in the simulation are difficult to observe directly. For example, the Mars Orbiter Laser Altimeter has detected a variety of aerosols but is relatively insensitive to tropical water ice clouds [*Neumann et al.*, 2003]. The situation is more complicated with TES, which sounds the atmosphere in both nadir and limb viewing geometries at local times of ~1400 and ~0200. Estimates for the column opacity of water ice can be extracted from nadir observations only on the dayside, where the relatively warm surface ($T > 220$ K) provides sufficient thermal contrast with the atmosphere [*Pearl et al.*, 2001; *Smith et al.*, 2001a]. In its limb scanning mode TES avoids this problem by observing the atmosphere against the cold background of deep space. Cloud opacity can then be retrieved at any local time accessible to observation, but only at altitudes above ~10 km where the data are free of contamination by surface thermal emission [*Christensen et al.*, 1998; *Pearl et al.*, 2001]. For these reasons, direct observations of low-lying nighttime cloud layers, such as those in Figures 12 and 13, may not be possible with TES.

[74] In our MGCM simulation, nighttime surface temperatures are enhanced at some locations by thermal emission from water ice clouds [cf. *Colaprete and Toon*, 2000, Figure 6; *Kieffer et al.*, 1977, Figure 16]. The spatial pattern of surface warming is correlated with the distribution of cloud opacity (Figure 6b), with the strongest effects in the Tharsis region. As part of an ongoing investigation, R. J. Wilson and M. D. Smith are testing this aspect of the simulation against TES observations of surface temperature at local times of ~0200 and ~1400. Their initial results provide tantalizing indirect evidence for the presence of a substantial nighttime cloud in the Tharsis region.

[75] These results illustrate the value of the MGCM as a tool for exploring interconnections among diverse observations. The relationships among the elevated temperature inversions observed by RS, the Tharsis morning cloud observed by terrestrial telescopes and HST, and nighttime surface temperature anomalies observed by TES will be examined more closely as part of future work.

References

Akabane, T., T. Nakakushi, K. Iwasaki, and S. M. Larson (2002), Diurnal variation of Martian water-ice clouds in Tharsis region of the low latitude cloud belt: Observations in 1995–1999 apparitions, *Astron. Astrophys.*, *384*, 678–688.

Andrews, D. G., J. R. Holton, and C. B. Leovy (1987), *Middle Atmosphere Dynamics*, 489 pp., Academic, San Diego, Calif.

Banfield, D., B. J. Conrath, M. D. Smith, P. R. Christensen, and R. J. Wilson (2003), Forced waves in the Martian atmosphere from MGS TES nadir data, *Icarus*, *161*, 319–345.

Christensen, P. R., et al. (1998), Results from the Mars Global Surveyor Thermal Emission Spectrometer, *Science*, *279*, 1692–1698.

Clancy, R. T., A. W. Grossman, M. J. Wolff, P. B. James, D. J. Rudy, Y. N. Billawala, B. J. Sandor, S. W. Lee, and D. O. Muhleman (1996), Water vapor saturation at low altitudes around Mars aphelion: A key to Mars climate?, *Icarus*, *122*, 36–62.

Clancy, R. T., B. J. Sandor, M. J. Wolff, P. R. Christensen, M. D. Smith, J. C. Pearl, B. J. Conrath, and R. J. Wilson (2000), An intercomparison of ground-based millimeter, MGS TES, and Viking atmospheric temperature measurements: Seasonal and interannual variability of temperatures and dust loading in the global Mars atmosphere, *J. Geophys. Res.*, *105*, 9553–9571.

Clancy, R. T., M. J. Wolff, and P. R. Christensen (2003), Mars aerosol studies with the MGS TES emission phase function observations: Optical depths, particle sizes, and ice cloud types versus latitude and solar longitude, *J. Geophys. Res.*, *108*(E9), 5098, doi:10.1029/2003JE002058.

Colaprete, A., and O. B. Toon (2000), The radiative effects of Martian water ice clouds on the local atmospheric temperature profile, *Icarus*, *145*, 524–532.

Colaprete, A., O. B. Toon, and J. A. Magalhães (1999), Cloud formation under Mars Pathfinder conditions, *J. Geophys. Res.*, *104*, 9043–9053.

Conrath, B. J., J. C. Pearl, M. D. Smith, W. C. Maguire, P. R. Christensen, S. Dason, and M. S. Kaelberer (2000), Mars Global Surveyor Thermal Emission Spectrometer (TES) observations: Atmospheric temperatures during aerobraking and science phasing, *J. Geophys. Res.*, *105*, 9509–9519.

Forget, F., F. Hourdin, R. Fournier, C. Hourdin, O. Talagrand, M. Collins, S. R. Lewis, P. L. Read, and J.-P. Huot (1999), Improved general circulation models of the Martian atmosphere from the surface to above 80 km, *J. Geophys. Res.*, *104*(E10), 24,155–24,175.

Glenar, D. A., R. E. Samuelson, J. C. Pearl, G. L. Bjoraker, and D. Blaney (2003), Spectral imaging of Martian water ice clouds and their diurnal behavior during the 1999 aphelion season ($L_s = 130°$), *Icarus*, *161*, 297–318.

Haberle, R. M., M. M. Joshi, J. R. Murphy, J. R. Barnes, J. T. Schofield, G. Wilson, M. Lopez-Valverde, J. L. Hollingsworth, A. F. C. Bridger, and J. Schaeffer (1999), General circulation model simulations of the Mars Pathfinder atmospheric structure investigation/meteorology data, *J. Geophys. Res.*, *104*, 8957–8974.

Hinson, D. P., and R. J. Wilson (2000), Measurements and simulations of tropical temperature inversions on Mars, *Bull. Am. Astron. Soc.*, *32*(3), 1091.

Hinson, D. P., and R. J. Wilson (2002), Transient eddies in the southern hemisphere of Mars, *Geophys. Res. Lett.*, *29*(7), 1154, doi:10.1029/2001GL014103.

Hinson, D. P., R. A. Simpson, J. D. Twicken, G. L. Tyler, and F. M. Flasar (1999), Initial results from radio occultation measurements with Mars Global Surveyor, *J. Geophys. Res.*, *104*, 26,997–27,012.

Hinson, D. P., G. L. Tyler, J. L. Hollingsworth, and R. J. Wilson (2001), Radio occultation measurements of forced atmospheric waves on Mars, *J. Geophys. Res.*, *106*, 1463–1480.

Hinson, D. P., R. J. Wilson, M. D. Smith, and B. J. Conrath (2003), Stationary planetary waves in the atmosphere of Mars during southern winter, *J. Geophys. Res.*, *108*(E1), 5004, doi:10.1029/2002JE001949.

Kieffer, H. H., T. Z. Martin, A. R. Peterfreund, B. M. Jakosky, E. D. Miner, and F. D. Palluconi (1977), Thermal and albedo mapping of Mars during the Viking primary mission, *J. Geophys. Res.*, *82*, 4249–4291.

Liu, J., M. I. Richardson, and R. J. Wilson (2003), An assessment of the global, seasonal, and interannual spacecraft record of Martian climate in the thermal infrared, *J. Geophys. Res.*, *108*(E8), 5089, doi:10.1029/2002JE001921.

Magalhães, J. A., J. T. Schofield, and A. Seiff (1999), Results of the Mars Pathfinder atmospheric structure investigation, *J. Geophys. Res.*, *104*, 8943–8955.

Neumann, G. A., D. E. Smith, and M. T. Zuber (2003), Two Mars years of clouds detected by the Mars Orbiter Laser Altimeter, *J. Geophys. Res.*, *108*(E4), 5023, doi:10.1029/2002JE001849.

Pearl, J. C., M. D. Smith, B. J. Conrath, J. L. Bandfield, and P. R. Christensen (2001), Observations of Martian ice clouds by the Mars Global Surveyor Thermal Emission Spectrometer: The first Martian year, *J. Geophys. Res.*, *106*, 12,325–12,338.

Pollack, J. B., R. M. Haberle, J. Schaeffer, and H. Lee (1990), Simulations of the general circulation of the Martian atmosphere: 1. Polar processes, *J. Geophys. Res.*, *95*, 1447–1473.

Richardson, M. I., and R. J. Wilson (2002a), A topographically forced asymmetry in the Martian circulation and climate, *Nature*, *416*, 298–301.

Richardson, M. I., and R. J. Wilson (2002b), Investigation of the nature and stability of the Martian seasonal water cycle with a general circulation model, *J. Geophys. Res.*, *107*(E5), 5031, doi:10.1029/2001JE001536.

Richardson, M. I., R. J. Wilson, and A. V. Rodin (2002), Water ice clouds in the Martian atmosphere: General circulation model experiments with a simple cloud scheme, *J. Geophys. Res.*, *107*(E9), 5064, doi:10.1029/2001JE001804.

Schofield, J. T., J. R. Barnes, D. Crisp, R. M. Haberle, S. Larsen, J. A. Magalhães, J. R. Murphy, A. Seiff, and G. Wilson (1997), The Mars Pathfinder atmospheric structure investigation/meteorology (ASI/MET) experiment, *Science*, *278*, 1752–1758.

Smith, D. E., et al. (2001), Mars Orbiter Laser Altimeter: Experiment summary after the first year of global mapping of Mars, *J. Geophys. Res.*, *106*(E10), 23,689–23,722.

Smith, M. D. (2002), The annual cycle of water vapor on Mars as observed by the Thermal Emission Spectrometer, *J. Geophys. Res.*, *107*(E11), 5115, doi:10.1029/2001JE001522.

Smith, M. D. (2004), Interannual variability in TES atmospheric observations of Mars during 1999–2003, *Icarus*, *167*, 148–165.

Smith, M. D., J. C. Pearl, B. J. Conrath, and P. R. Christensen (2001a), Thermal Emission Spectrometer results: Mars atmospheric thermal structure and aerosol distribution, *J. Geophys. Res.*, *106*(E10), 23,929–23,945.

Smith, M. D., J. C. Pearl, B. J. Conrath, and P. R. Christensen (2001b), One Martian year of atmospheric observations by the Thermal Emission Spectrometer, *Geophys. Res. Lett.*, *28*(22), 4263–4266.

Toon, O. B., C. P. McKay, T. P. Ackerman, and K. Santhanam (1989), Rapid calculation of radiative heating rates and photodissociation rates in inhomogeneous multiple scattering atmospheres, *J. Geophys. Res.*, *94*, 16,287–16,301.

Tyler, G. L., G. Balmino, D. P. Hinson, W. L. Sjogren, D. E. Smith, R. A. Simpson, S. W. Asmar, P. Priest, and J. D. Twicken (2001), Radio science observations with Mars Global Surveyor: Orbit insertion through one Mars year in mapping orbit, *J. Geophys. Res.*, *106*(E10), 23,327–23,348.

Wang, H., and A. P. Ingersoll (2002), Martian clouds observed by Mars Global Surveyor Mars Orbiter Camera, *J. Geophys. Res.*, *107*(E10), 5078, doi:10.1029/2001JE001815.

Wilson, R. J. (1997), A general circulation model simulation of the Martian polar warming, *Geophys. Res. Lett.*, *24*, 123–126.

Wilson, R. J. (2000), Evidence for diurnal period Kelvin waves in the Martian atmosphere from Mars Global Surveyor TES data, *Geophys. Res. Lett.*, *27*, 3889–3892.

Wilson, R. J. (2002), Evidence for nonmigrating thermal tides in the Mars upper atmosphere from the Mars Global Surveyor Accelerometer Experiment, *Geophys. Res. Lett.*, *29*(7), 1120, doi:10.1029/2001GL013975.

Wilson, R. J., and K. Hamilton (1996), Comprehensive model simulation of thermal tides in the Martian atmosphere, *J. Atmos. Sci.*, *53*, 1290–1326.

Wilson, R. J., and M. I. Richardson (2000), The Martian atmosphere during the Viking Mission, 1. Infrared measurements of atmospheric temperatures revisited, *Icarus*, *145*, 555–579.

Wilson, R. J., D. Banfield, B. J. Conrath, and M. D. Smith (2002), Traveling waves in the Northern Hemisphere of Mars, *Geophys. Res. Lett.*, *29*(14), 1684, doi:10.1029/2002GL014866.

Wilson, R. J., D. Banfield, D. Hinson, and M. D. Smith (2003), GCM simulation of thermal tides in the Mars atmosphere, paper presented at International Workshop: Mars Atmosphere Modelling and Observations, Eur. Space Agency, Granada, Spain, 13–15 Jan. 2003.

Wolff, M. J., and R. T. Clancy (2003), Constraints on the size of Martian aerosols from Thermal Emission Spectrometer observations, *J. Geophys. Res.*, *108*(E9), 5097, doi:10.1029/2003JE002057.

Zurek, R. W. (1976), Diurnal tide in the Martian atmosphere, *J. Atmos. Sci.*, *33*, 321–337.

Zurek, R. W., J. R. Barnes, R. M. Haberle, J. B. Pollack, J. E. Tillman, and C. B. Leovy (1992), Dynamics of the atmosphere of Mars, in *Mars*, edited by H. H. Kieffer et al., pp. 835–933, Univ. of Ariz. Press, Tucson.

————————————

D. P. Hinson, Department of Electrical Engineering, Stanford University, 350 Serra Mall, Stanford, CA 94305, USA. (hinson@rocc.stanford.edu)

R. J. Wilson, Geophysical Fluid Dynamics Laboratory (NOAA), Princeton University, Forrestal Campus, P.O. Box 308, Princeton, NJ 08542, USA. (rjw@gfdl.noaa.gov)